Supporting Information for "Quantifying the impact of bedrock topography uncertainty in Pine Island Glacier projections for this century"

Andreas Wernecke[1,2,3], Tamsin L. Edwards[4], Philip B. Holden[1], Neil R. Edwards[1], Stephen L. Cornford [5]

[1]The Open University, Milton Keynes, UK

[2]Max-Planck-Institute for Meteorology, Hamburg, Germany

[3]Universitt Hamburg, Hamburg, Germany

[4]Kings Collage London, London, UK

[5]Faculty of Science and Engineering, Swansea University, Swansea, UK

Contents of this file

1. Text S1 to S5
2. Figures S1 to S6
3. Table S1

Additional Supporting Information (Files uploaded separately)

1. Movie S1 to S4

Text S1.

1. RES data inconsistencies

By careful inspection we asses the consistency of the radio echo sounding data. In particular we inspect the ice thickness estimates and search for (1) sudden and sustained changes along flight lines (e.g. as highlighted at the bottom of Figure S1) and (2) sections of flight line ice thickness estimates which cross several other flight lines and have sustained different values (e.g. as highlighted in the center of Figure S1). These two criteria are often found in conjunction. Note that Figure S1 is not the final dataset used here, but illustrates the process of identifying inconsistencies.

Text S2.

2. Statistical properties of the bedrock topography

The information in this section is taken from Wernecke (2020), with minor adjustments, and repeated here for the readers' convenience.

2.1. Gaussian Process modelling

In the following we will describe our approach to generating new bedrock topographies in more detail. The main novelty is that we use a stochastic model to represent the bedrock topography at each location as a random variable and represent uncertainties in these random variables (the spread) by sampling spatial fields of bedrock topography which inhabit the local uncertainties and spatial covariance structure.

The bedrock can be understood as continuous random variable B, approximated as a Gaussian Process,

$$B = G(\vec{\bar{b}}(\vec{z}, \vec{\theta}),\ c(\vec{\theta})), \tag{1}$$

where $G(\cdot, \cdot)$ denotes a Gaussian Process. The bedrock topography at each location in the horizontal model domain is therefore considered a random variable with Gaussian distribution centered at $\vec{\bar{b}}(\vec{z}, \vec{\theta})$, depending on the observations $\vec{z}$ with covariance between locations defined by the covariance function $c(\vec{\theta})$. The covariance function parameters $\vec{\theta}$ define among other things the length scale of decorrelation, or in other words, how informative the topography at one location is for the topography at surrounding locations. We do not use a reference topography as prior nor do we subtract any mean function in order to ensure independence from all published datasets. This will allow us to investigate the consistency between the topographies statistically generated here and reference topographies (Bedmap2 and Bedmachine) in the following analysis.

We assume the existence of an optimal set of covariance function parameters $\vec{\theta^*}$ and constrain estimates of $\vec{\theta^*}$ with observations. To asses these covariance function parameters we will in this section describe the analysis in more detail than possible in the main text. Using conditional likelihoods we can express Equation 1 as:

$$B = G(\vec{\bar{b}}(\vec{z}, \vec{\theta^*}),\ c(\vec{\theta^*}))\, |\vec{\theta^*} \cdot \pi(\vec{\theta^*}|\vec{z}) \cdot \pi(\vec{z}) \tag{2}$$

Due to computational constraints we have to use subsets of the whole set of observations ($\vec{z}$), with $\vec{z_1}$ of $\mathcal{O}(10\,000)$ measurements for $\vec{\bar{b}}(\vec{z}, \vec{\theta^*})$ and $\vec{z_2}$ of $\mathcal{O}(100\,000)$ for $\pi(\vec{\theta^*}|\vec{z})$. The reason for the different sample sizes is that the computational expense associated with

the size of $\vec{z_1}$ is of $\mathcal{O}(n^3)$ the expense associated with the size of $\vec{z_2}$ is of $\mathcal{O}(n^2)$ (see below). Equation 2 becomes:

$$B = G(\vec{\bar{b}}(\vec{z_1}, \vec{\theta^*}),\ c(\vec{\theta^*}))\,|\vec{\theta^*} \cdot \pi(\vec{\theta^*}|\vec{z_2}) \cdot \pi(\vec{z_2}) \tag{3}$$

We constrain $\pi(\vec{\theta^*}|\vec{z_2})$ using semivariograms. In semivariograms the distances between all possible pairs of $\vec{z_2}$ are binned, in our case in 250 m intervals and the covariance between all pairs within each interval is calculated. It therefore illustrates how the correlation in topography elevation diminishes with distance and can be used to infer the nugget (variance at a distance of zero), range (characteristic correlation length scale) and sill (far field variance) by a least squared error fit. We use an exponential function for the semivariogram fit and the covariance function of the GP model which allows us to use the fitted parameters as our best estimate of θ^*. A limitation of using semivariograms to find the covariance function is the possible dependency of $\pi(\vec{\theta^*}|\vec{z_2})$ on the size of the domain examined for the semivariograms. This additional uncertainty is taken into account by using six different domains, from [0 km, 25 km] to [0 km, 50 km] (see Figure S2). That is from the approximate width of contributory glaciers of PIG (25 km) to approximately the largest data gap between flight-lines in the catchment area (50 km). The spatial characteristics on scales larger than this will be well constrained by the observations themselves. Note that the range parameter can lie outside of this domain, as this is merely the domain used for fitting. The total number of pairs n samples can build is $n(n-1)/2$, which explains why the computational cost of semivariograms scales with $\mathcal{O}(n^2)$.

The distribution of $\pi(\vec{z_2})$ is represented by repeated random sub-sampling of $\vec{z_2}$ from $\vec{z}$. Six different sets of $\vec{z_2}$ are then used for $\pi(\vec{\theta^*}|\vec{z_2})$ together with six different fitting domains, increasing the upper bound in 5 km steps from 25 to 50 km to represent the distribution of $\pi(\vec{\theta^*}|\vec{z_2})$. The six resulting semivariograms are shown in Figure S2 and the corresponding estimates of θ^* are shown in Table S1. The relatively small spread of estimates of θ^* (Table S1) illustrates that the combined impact of sub-sampling and fitting interval size on θ^* is small, supporting the robustness of this approach. All those estimates are used successively for the GP model $G(\vec{b}(\vec{z_1}, \vec{\theta^*}),\ c(\vec{\theta^*}))\,|\vec{\theta^*}$ (technically these are six separate GP models which are handled in the same way at all times). In order to ensure good spatial coverage by $\vec{z_1}$ we impose a regular grid with 2 km resolution on the region and randomly select one measurement from each non-empty grid cell. This semi-random selection is repeated for each estimate of θ^*.

To address the correspondence of parameters from the semivariogram fit and the covariance function it can be illustrative to discuss particularly the role of σ_c^2. It is derived as the sill of the exponential fit to the semivariance, representing the semivariance at large distances where spatial correlations are negligible and enters the covariance function as scaling parameter of the exponentially decaying covariance. For very small distances r, $COV(x_i, x_i) \approx \sigma_c^2$. The covariance of the topography at x_i with x_i is simply the variance at this location. The semivariance (y) for a given distance (r) between the locations x_i and x_j is defined as: $y(x_i, x_j) = 0.5 \cdot VAR(f(x_i) - f(x_j))$, where $f()$ represents the mapping of locations to topography values. For locations far from each other ($r \gg \ell$) the topography

is considered uncorrelated so that the semivariance simplifies to:

$$y(x_i, x_j) = 0.5 \cdot VAR(f(x_i)) + 0.5 \cdot VAR(f(x_j)).$$

We have seen before that for our covariance function, the variance at x_i approaches σ_c^2, so that $y(x_i, x_j) = \sigma_c^2$ if x_i and x_j are far from each other. Therefore the parameter σ_c in the covariance function can be approximated by the sill of the semivariance. In other words, the semivariance is reduced where the covariance is still large, but the maximum semivariance (σ_c^2) informs the total variance which is defined by the covariance at very small r.

Considering a set of training point locations $\vec{x_1}$ with corresponding topography values $\vec{z_1}$, the random distribution of a GP model at a new, finite set of locations $\vec{x_*}$ is found (see e.g. Rasmussen and Williams (2006)) by:

$$G(\vec{\bar{b}}(\vec{z_1}, \vec{\theta^*}),\ c(\vec{\theta^*})) = N(\vec{\bar{b}}(\vec{z_1}, \vec{\theta^*}), \mathbf{\Sigma}_*) \tag{4}$$

$$\vec{\bar{b}}(\vec{z_1}, \vec{\theta^*}) = K(\vec{x_*}, \vec{x_1})K(\vec{x_1}, \vec{x_1})^{-1}\vec{z_1} \tag{5}$$

$$\mathbf{\Sigma}_* = K(\vec{x_*}, \vec{x_*}) - K(\vec{x_*}, \vec{x_1})K(\vec{x_1}, \vec{x_1})^{-1}K(\vec{x_1}, \vec{x_*})) \tag{6}$$

where $N(\vec{\mu}, \mathbf{\Sigma})$ represents a multivariate normal distribution with mean vector $\vec{\mu}$ and covariance matrix $\mathbf{\Sigma}$. The values of $K(\vec{x}, \vec{x})_{ij} = c(\vec{x_i}, \vec{x_j})$ are derived from evaluations of the GP covariance function $c(\cdot, \cdot)$ of the ith and jth member of $\vec{x}$ (see covariance equation in the main text). The diagonal of $\mathbf{\Sigma}_*$ is the total variance at locations $\vec{x_*}$, as shown, in terms of its square root, in Figure 1(a) and shading in Figure S5.

2.2. GP samples

For the application in this work it is essential that the samples from the Gaussian Process (GP) are continuous so that no unreasonable jumps in the topography are created. The only way to ensure continuous samples, representing the full PIG topography covariance structure is to avoid any subdivision of the PIG basin in the topography generation process. As will be shown in the following, this influences the numerical demands and achievable topography resolution of this approach.

We use the GPy Python toolbox (specifically: posterior_samples_f()) to generate those samples. It is however informative to follow Rasmussen and Williams (2006, Section A.2) to give a short introduction on how samples can be generated without a specific toolbox. A scalar random number generator and an implementation of a Cholesky decomposition algorithm will be assumed, both widely available in mathematical software. First we use the Cholesky decomposition to find the lower triangular matrix L for the positive-definite symmetric covariance matrix $\mathbf{\Sigma}_G$ which satisfies $LL^T = \mathbf{\Sigma}_G$. $\mathbf{\Sigma}_G$ is the GP covariance matrix with element i,j: $\mathbf{\Sigma}_{G,i,j} = COV(x_i, x_j)$. We then generate n_* independent standard-normally distributed random numbers stacked to the vector $\vec{p}$ where n_* is the number of evaluation points $\vec{x_*}$. A sample of the distribution G is then found by $\vec{o_*} = \vec{\mu}_G + L\vec{p}$, where $\vec{\mu}_G$ is the mean field of the GP. By construction the covariance matrix of $\vec{o_*}$ is $\mathbf{E}[\vec{o_*}\vec{o_*}^T] = L\mathbf{E}[\vec{p}\vec{p}^T]L^T = LL^T = \mathbf{\Sigma}_G$. Cholesky decompositions scale with order n^3, creating comparable restrictions for the number of training data for GPs without additional approximations and evaluation locations of GP samples. On modern workstations this limit is of the order of a few 10 000 evaluation locations.

Text S3.

3. Model Inversion

The information in this section is taken from Wernecke (2020), with minor adjustments, and repeated here for the readers' convenience.

Each topography is used separately to find basal traction coefficient and effective viscosity fields for PIG using the BISICLES inverse model framework with surface velocities from (Rignot et al., 2017, 2011) which have been re-gridded from 450 m to 1 km resolution using bilinear interpolation. The velocity data have been compiled from a large range of satellite missions, spanning in total the period from 1996 to 2016. It should however be noted that the data acquisition is not homogeneous throughout time. For example, only two of eight satellite missions used provide any data before 2006 and the start of the Landsat-8 and Sentinel-1 missions in 2013/2014 creates elevated data density towards the end of the 20-year period.

All datasets used for model inversion and initialisation are collected relatively close to the the year 2000 and even though a robust definition of a start year is challenging, the timestamp of the SMB forcing allows us to date the start of the simulations to year 2000 AD.

We use a linear Weertman friction law for inversions as in our experience it increases numerical stability in the optimisations compared with nonlinear Weertman friction laws. The effective viscosity is not influenced by the friction law but the inverted fields of basal traction coefficients have to be transformed to nonlinear equivalents as described below. The Weertman friction law is:

$$\tau_b = C_m \cdot |u_b|^{m-1} \cdot u_b$$

with $m = 1$ for linear friction, $m = 1/3$ for nonlinear friction and $m = 1/8$ for strongly nonlinear friction. In the following we will refer to the $m = 1/8$ friction law as plastic friction law (see also Joughin, Smith, and Schoof (2019)). Here τ_b is the basal stress tangential to the base of the ice, C_m is the spatially varying basal traction coefficient for a given friction law exponent m and u_b is the basal ice velocity. With the optimal initial basal shear stress τ_b being independent of the friction law it follows that

$$C_1 \cdot |u_{b0}|^0 \cdot u_{b0} = C_{1/3} \cdot |u_{b0}|^{(-2/3)} \cdot u_{b0}$$

and hence $C_{1/3} = C_1 |u_{b0}|^{(2/3)}$, where u_{b0} is the basal velocity at the beginning of the model period (as used for the inversion). An equivalent transformation is performed for plastic friction with $m = 1/8$.

Ice flow outside of the catchment area is expected to have minimal influence on the PIG flow. Therefore we drastically increase the basal traction coefficient for all friction laws to 10^6 Ns m^{-3} for grounded areas outside of the catchment area to effectively prevent ice from flowing. This is done for numerical stability at the quadratic domain boundaries and for numerical speed since suppressed ice flow allows the adaptive mesh to use lower resolutions.

Text S4.

4. Initial model behaviour

The information in this section is taken from Wernecke (2020), with minor adjustments, and repeated here for the readers' convenience.

Here we address the initial model behaviour and define a reference year for later projections. Figure S3 shows the yearly change in ice thickness (ds/dt, based on finite differences of the yearly data) for one of the randomly generated ensemble members (set B_r) with low forcing and plastic friction as an example. In the first years we see high-amplitude small-spatial-scale rates of ice thickness change which diminish with time to larger scale rates with smaller amplitude (as can be seen for year 15 of the simulation in Figure S3). These initial very high rates of ice thickness change can be attributed to an adjustment of the model to a self-consistent state. It indicates that, before adjusting, the flow regime and geometry are initially inconsistent with the model physics. The challenge here is to define the time when the persistent response dominates over the initial adjustments.

In retrospect we should have implemented a spin-up period in the simulations with a constant forcing (ocean melt and SMB) for the model to find a self-consistent state before the forced projections start. Instead the imposed SMB in all of our simulations use estimates for year 2000 in the beginning of the simulations which is why we define the beginning of the simulations as year 2000. In the same way, the basal melt starts to increase from the first year in the high forcing runs. In the following we will instead define a reference year which is used as baseline for calculations, e.g. of sea level rise contributions, in order to minimize the impact of initial adjustments on the results.

Defining a reference year by inspecting each of the 84 ensemble members (12+2 topographies times two forcings and three friction laws) in the style of Figure S3 is impractical. Therefore we calculate the spatial mean of the absolute ds/dt values and plot the development for each ensemble member using a B_r, Bedmap2 or BedMachine topography in Figure S4. Following a maximum ice thickness change in the first year, all ensemble members level out to a stable rate after a few decades or less. Bedmap2 and BedMachine start from slightly lower values in the beginning but take a similar period of time to reach a stable rate. It is not clear whether this slightly reduced period of adjustment indicates a more consistent initial state or reflects the smoother nature of those topographies. Based on Figure S4 we choose the 15th year of simulation as reference and consider this a conservative (on the larger end) value.

Text S5.

5. Possible explanations for the outlier behaviour of Bedmap2 simulations

In this section we discuss possible explanations for the outlier behaviour of Bedmap2 simulations, which remain in a steadily evolving state even for strong increasing ocean melt and RCP8.5 SMB. As stated in the main text, we cannot conclusively identify the cause of this behaviour but can show that there is no particular topographic height or feature in the basal friction field that offers a likely explanation.

5.1. Comparison of the topographic maps

Figure S5 shows all topographies used here, and the GP mean field, which was not used for the simulations. It can be seen that the GP mean and Bedmachine agree well along this flowline. Bedmap2 largely follows the same shape but is some 50 m higher. In two

dimensions (Figure S6) a similar picture emerges. The average of the statistically generated fields is largely below Bedmap2 but this offset is relatively homogeneous within the main trunk of PIG (along the line in Figure S6, left). There are only sporadic locations where Bedmap2 is above (red) or below (blue) all individual members of the statistically generated ensemble (Figure S6, right). There are a few grid cells where Bedmap2 is higher than all statistically generated topographies (red cells highlighted by orange frame in Figure S6, right) which resembles what could be interpreted as topographic elevation crossing the PIG trunk. However these consist of only approximately three grid cells which are not always adjacent. In fact, this corresponds not to a topographic high but a local depression which is also highlighted by an orange line in Figure S5 about 20 km upstream of the GL. A less deep depression in Bedmap2 compared to the other topographies is not as straightforward to associate dynamically with flow stabilization than a topographic high. Nevertheless, Nias, Cornford, and Payne (2018) argue that a small regional depression (20-30 m in amplitude, 4 km in diameter) can cause an dynamic thinning impulse which propagates upstream and is sustained even when another stabilising GL location is reached.

Figure 2 in the main text shows a topographic high near the GLs of the statistically generated topographies and Bedmap2. Considering the different behaviour of simulations on those topographies, this rise is not a defining factor for the response. This seems to be because the topographic high is hardly in contact with the ice in the first place. This could (but does not have to be) a sign that the reason for Bedmap2 to have this topographic high is the misclassification of RES reflection from the bottom of a floating ice shelf as

topographic reflections from grounded ice. In that case the base of the falsely assumed-grounded ice would coincide with the hydrostatic equilibrium and hence unground very easily. The statistically generated topographies have the same topographic high because they use the Bedmap2 geometry where no clear contact with the ground can be established. We use the Bedmap2 ice shelf mask to distinguish between grounded and ungrounded locations in the topography generation process, which is derived directly from satellite observations.

5.2. Basal friction coefficient

All topographies have their own inversion for basal friction coefficients which are held constant for the simulations. In the supplemented media (.gif) files we show animations of the grounding line retreating within the 100-year long simulations for Bedmap2, Bedmachine and two statistically generated topographies along with the basal friction coefficients (in all cases with strongly nonlinear friction law and strong forcing). This highlights the existence of linear features across the PIG trunk in all cases and shows how the retreat of the corresponding grounding lines is influenced by these features. The initial situation for the statistically generated topographies and Bedmap2 is such that the closest linear feature of high friction is not close to the grounding line. For the statistically generated topograpies the retreat is much faster and widespread, not through a specific gap in a high-friction feature, while for Bedmap2 there is limited retreat. The initial Bedmachine GL is much closer to a linear high friction feature compared to the other topographies used, the grounding line subsequently retreats, starting at the southern side of the ice stream and settling temporarily at a second, upstream high-friction feature later in the

simulation. Again, we cannot identify a particular feature in the friction coefficient that would be a likely explanation for the difference in simulation behaviour.

We further note that the Bedmap2 topography lies largely above the others within the first approximately 150 km upstream from the GL (Figure S5) and that, for the same surface elevation of the ice, an elevated topography is further from hydrostatic equilibrium and could hence be less prone to retreat. The about 50 m difference in ice thickness corresponds to an additional couple of metres of ice which need to be removed before ungrounding, which is small compared to the locally more than 250 m of melt per year. This indicates that the, on average, higher Bedmap2 topography and its corresponding thinner ice thickness alone is not a likely explanation for the outlier behaviour of Bedmap2 simulations either.

References

Holt, J. W., Blankenship, D. D., Morse, D. L., Young, D. A., Peters, M. E., Kempf, S. D., ... Corr, H. F. (2006). New boundary conditions for the west antarctic ice sheet: Subglacial topography of the thwaites and smith glacier catchments. *Geophysical Research Letters*, *33*(9), L09502. doi: 10.1029/2005GL025561

Joughin, I., Smith, B. E., & Schoof, C. G. (2019). Regularized coulomb friction laws for ice sheet sliding: Application to pine island glacier, antarctica. *Geophysical Research Letters*, *46*(9), 4764–4771. doi: 10.1029/2019GL082526

Nias, I. J., Cornford, S., & Payne, A. (2018). New mass-conserving bedrock topography for pine island glacier impacts simulated decadal rates of mass loss. *Geophysical Research Letters*, *45*(7), 3173–3181. doi: 10.1002/2017GL076493

Paden, J., Li, J., Leuschen, C., Rodriguez-Morales, F., & Hale, R. (2010). Icebridge mcords l2 ice thickness, version 1. from oct. 2009 to dec. 2017. Boulder, Colorado USA. NASA National Snow and Ice Data Center Distributed Active Archive Center. (updated 2019, Accessed: 2019-09) doi: 10.5067/GDQ0CUCVTE2Q

Rasmussen, C. E., & Williams, C. K. (2006). *Gaussian processes for machine learning* (Vol. 2) (No. 3). MIT Press Cambridge, MA.

Rignot, E., Mouginot, J., & Scheuchl, B. (2017). Measures insar-based antarctica ice velocity map, version 2. Boulder, Colorado USA. NASA National Snow and Ice Data Center Distributed Active Archive Center. (Accessed: 2018-11) doi: 10.5067/D7GK8F5J8M8R

Rignot, E., Velicogna, I., van den Broeke, M. R., Monaghan, A., & Lenaerts, J. T. (2011). Acceleration of the contribution of the greenland and antarctic ice sheets to sea level rise. *Geophysical Research Letters*, *38*(5), L05503. doi: 10.1029/2011GL046583

Wernecke, A. (2020). *Quantifying century-scale uncertainties of the global mean sea level rise contribution from the amundsen sea sector, west antarctica* (Doctoral dissertation, The Open University). doi: 10.21954/ou.ro.0001223d

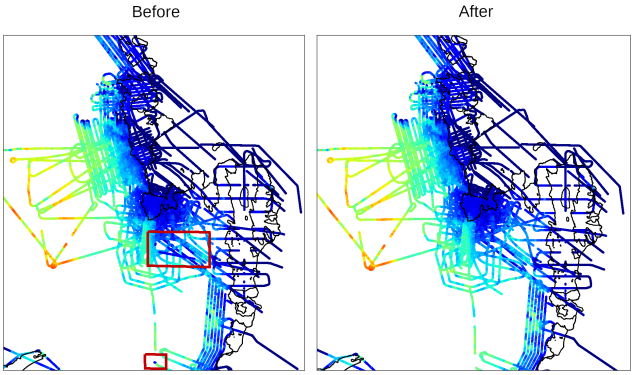

Figure S1. Ungridded RES ice thickness estimates (from zero - dark blue to 2300 m - red) before (left) and after (right) removal of some inconsistent data. Locations inconsistent data are highligterd by red rectangles. Data from Holt et al. (2006) and Paden et al. (2010)

Table S1. Estimates of $\vec{\theta^*}$

	θ^*_{25}	θ^*_{30}	θ^*_{35}	θ^*_{40}	θ^*_{45}	θ^*_{50}
Fitting interval [km]	25	30	35	40	45	50
Nugget σ_n^2 $[m^2]$	563	647	652	477	583	661
Range ℓ [km]	19	18	18	17	19	20
Sill α^2 $[\times 10^3 m^2]$	82	82	79	79	83	86

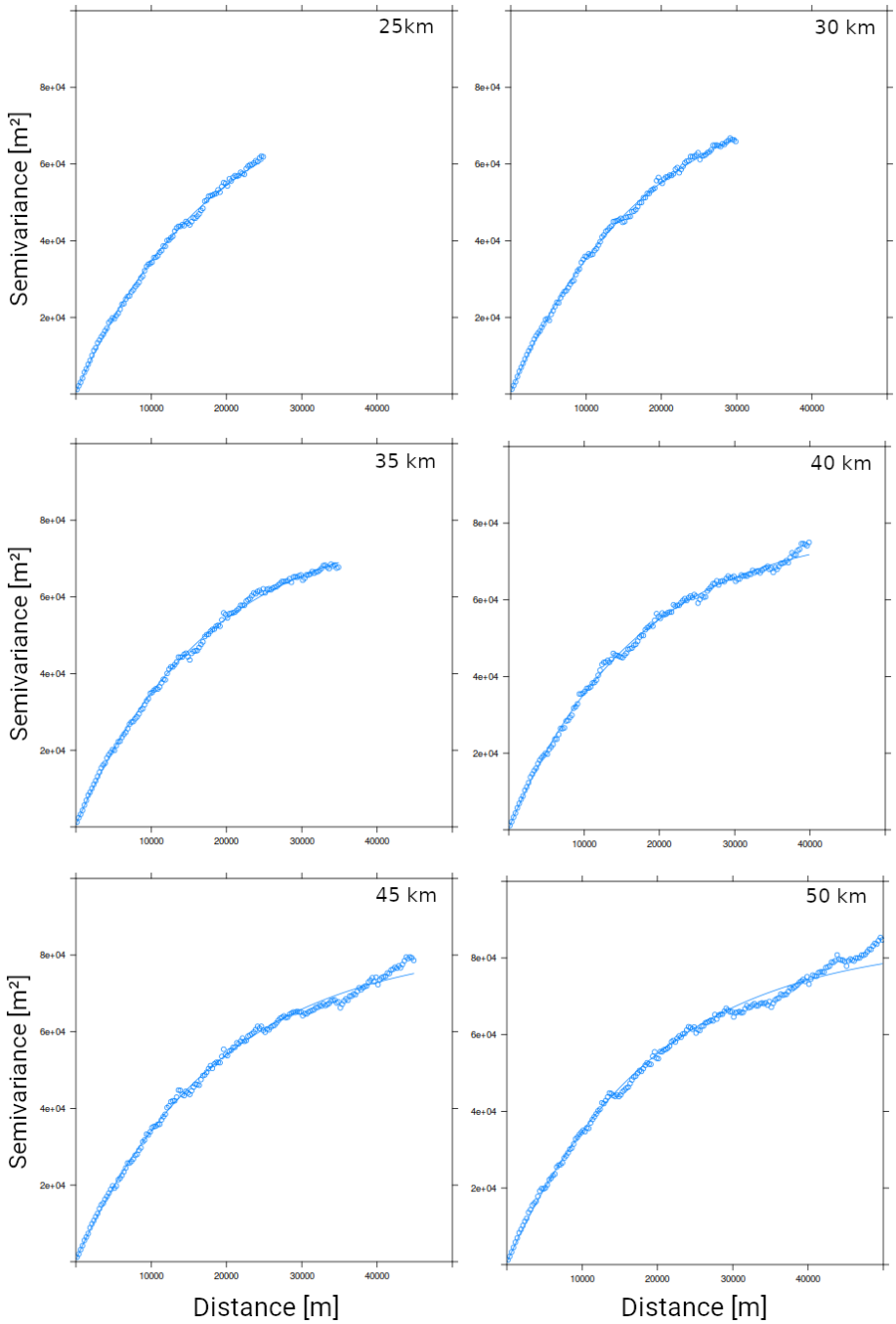

Figure S2. Semivariograms of bedrock topography for Pine Island Glacier from ungridded airborne RES observations described in the main text with exponential least-squared-error fits (lines). Different fitting intervals are used (as quoted in each panel) to investigate the impact of the fitting interval on the parameter values, which are shown in Table S1.

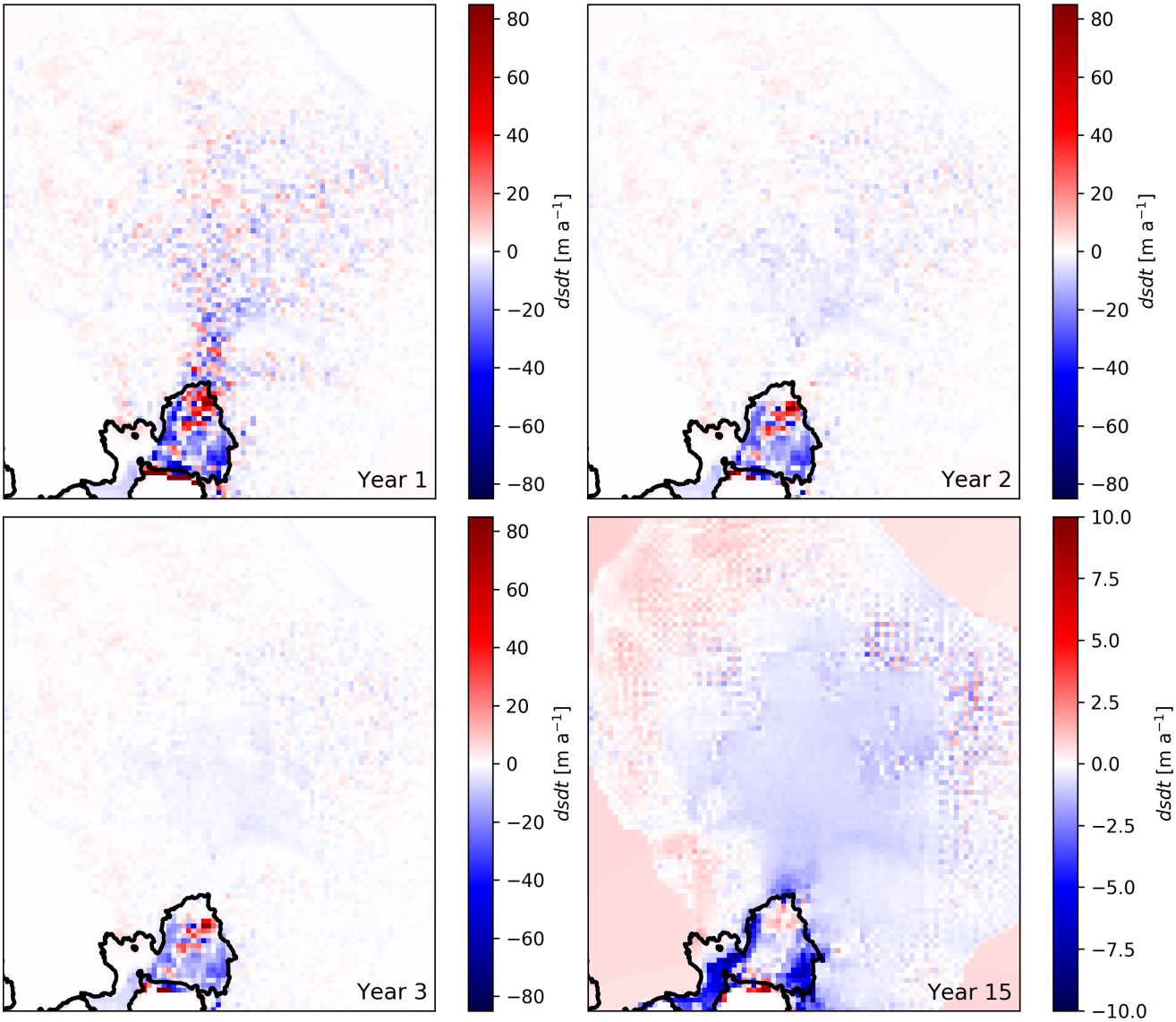

Figure S3. Ice thickness change across PIG model domain in the beginning of the simulations after initializing with velocity data from 1996 to 2016 (years of simulation shown in the lower right corners). Based on a statistically generated topography (B_r #5) with low forcing and plastic friction. Note the smaller colour range in the lower right panel.

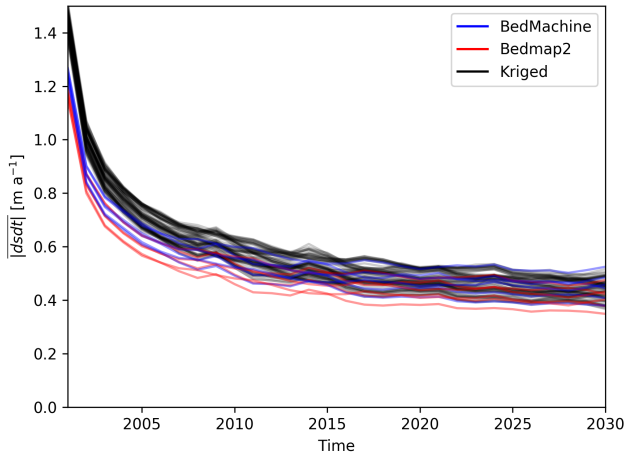

Figure S4. Spatial mean of absolute ice thickness change across PIG model domain for the beginning of the simulations. The initial drop can be associated with BISICLES adjusting to a self-consistent state.

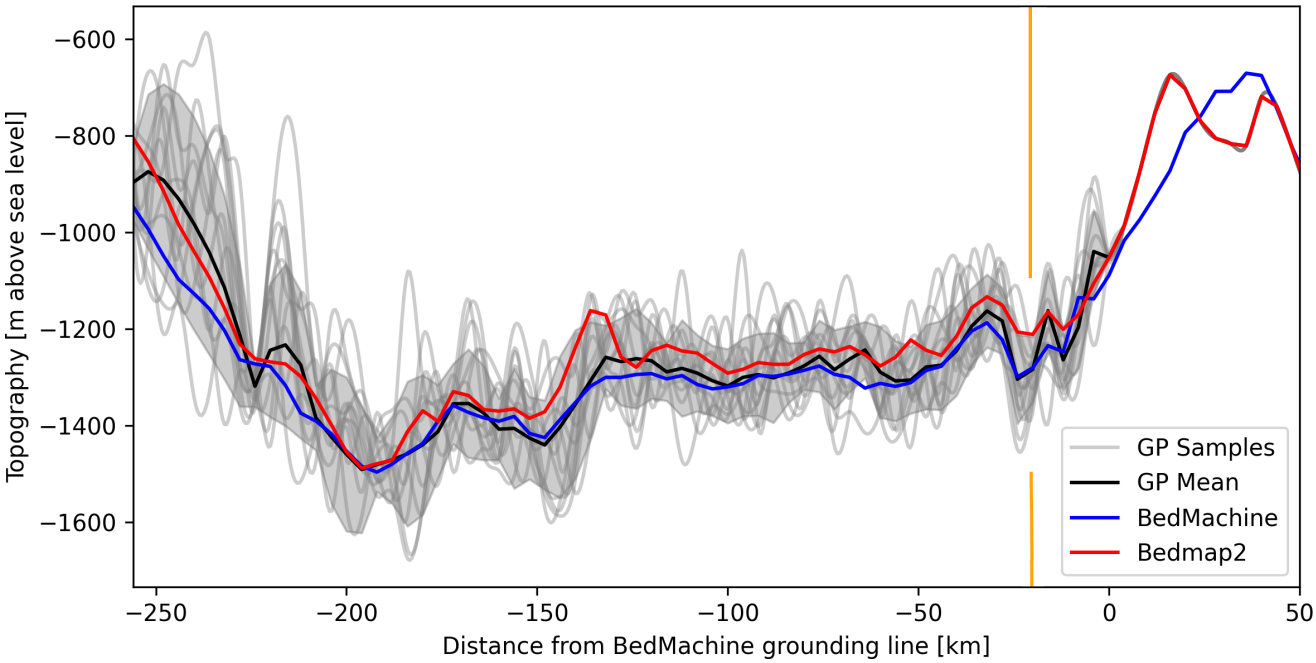

Figure S5. Bedrock topographies on 4 km resolution for Bedmap2, BedMachine, 12 topographies statistically generated here (B_r; for illustration interpolated with a quadratic spline) and the GP model trained on 30 km domain for which shading illustrates $\pm\sigma$. The cross-section roughly follows the center of PIG, as shown in Figure 1 in the main text from point A (left) to point D (right). Grounding line location (x=0) is based on BedMachine geometry which coincides for this section with the extent of the GP models. Under the ice shelf (as defined by Bedmap2) the topographies statistically generated here use the Bedmap2 topography. The orange line highlights a location mentioned in the text.

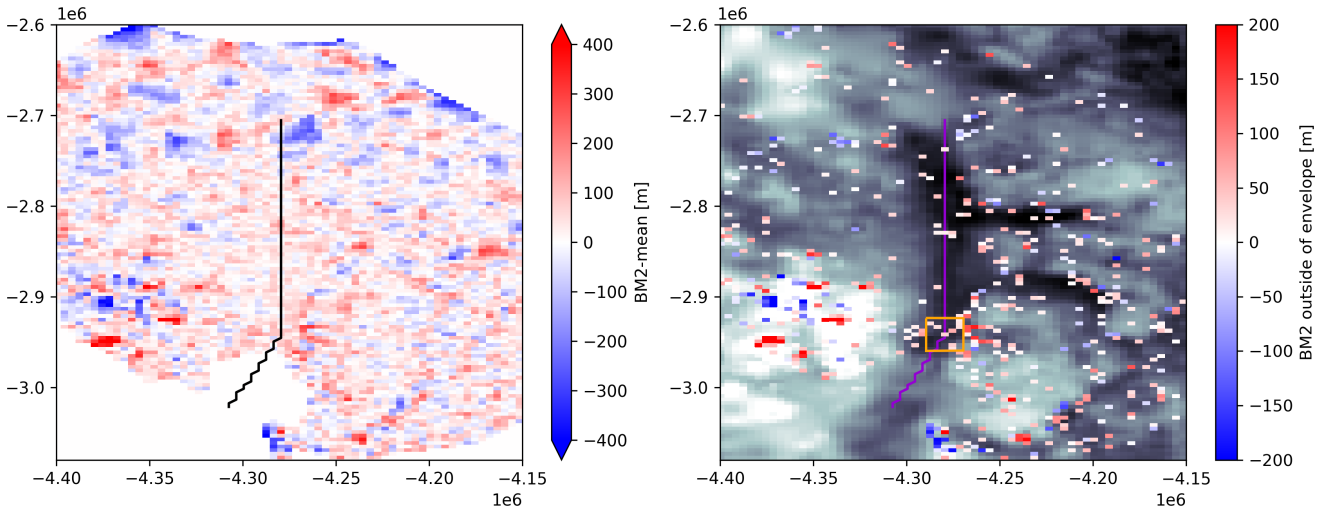

Figure S6. Left: Difference of Bedmap2 and the mean of all statistically generated topographies used here. Right: Difference between Bedmap2 and the closest member of the statistically generated ensemble where Bedmap2 is outside of the envelope of those topographies. At locations where Bedmap2 lies within the range of the statistically generated topographies, the Bedmap2 topography itself is shown (grey shading in background). For comparison, the central flow line of PIG as in Figure 1 in the main text. The orange frame highlights a region mentioned in the text.

6. Additional Supporting Information (Files uploaded separately)

Movie S 0.1. Basal stress parameter τ_b in Pa. Where ice is ungrounded the basal friction is set to zero, otherwise the parameter from the initial model inversion is shown. The animation shows the retreat of the grounded ice by an expansion of zero valued τ_b over 100 years (also highlighted by black line) with Weertman friction law and exponent of $m = 1/8$ and Bedmap2 topography.

Movie S 0.2. as Movie S0.1 but for BedMachine topography.

Movie S 0.3. as Movie S0.1 but for statistically generated topography 'Br001'.

Movie S 0.4. as Movie S0.1 but for statistically generated topography 'Br002'.